catalysts

MDPI

Article

Ordered Mesoporous nZVI/Zr-Ce-SBA-15 Catalysts Used for Nitrate Reduction: Synthesis, Optimization and Mechanism

Ruimin Zhang [1,*], Haixia Liu [1], Weili Jiang [2] and Weijing Liu [2]

[1] School of Environment and Ecology, The City Vocational College of Jiangsu, Nanjing 210019, China; liuhaixia198027@126.com
[2] Jiangsu Province Key Laboratory of Environmental Engineering, Nanjing 210019, China; jiangweili@yeah.net (W.J.); liuwj@jshb.gov.cn (W.L.)
* Correspondence: zhangruimin_04@163.com; Tel.: +86-159-5056-8032

Abstract: Excessive concentrations of nitrate (NO_3-N) in water lead to the deterioration of water quality, reducing biodiversity and destroying ecosystems. Therefore, the present study investigated NO_3-N removal from simulated wastewater by nanoscale zero-valent iron-supported ordered mesoporous Zr-Ce-SBA-15 composites (nZVI/Zr-Ce-SBA-15) assisted by response surface methodology (RSM), an artificial neural network combined with a genetic algorithm (ANN-GA) and a radial basis neural network (RBF). The successful support of nZVI on Zr-Ce-SBA-15 was confirmed using XRD, FTIR, TEM, SEM–EDS, N_2 adsorption and XPS, which indicated ordered mesoporous materials. The results showed that ANN-GA was better than the RSM for optimizing the conditions of NO_3-N removal and the RBF neural network further confirmed the reliability of the ANN-GA model. The removal rate of NO_3-N by the composites reached 95.71% under the optimized experimental conditions (initial pH of 4.89, contact time = of 62.27 min, initial NO_3-N concentration of 74.84 mg/L and temperature of 24.77 °C). The process of NO_3-N adsorption onto Zr-Ce-SBA-15 composites was followed by the Langmuir model (maximum adsorption capacity of 45.24 mg/g), pseudo-second-order kinetics, and was spontaneous, endothermic and entropy driven. The yield of N_2 can be improved after nZVI was supported on Zr-Ce-SBA-15, and the composites exhibited a strong renewability in the short term within three cycles. The resolution of Fe^{2+} experiments confirmed that nZVI/Zr-Ce-SBA-15 was simultaneously undergoing adsorption and catalysis in the process of NO_3-N removal. Our study suggests that the ordered mesoporous nZVI/Zr-Ce-SBA-15 composites are a promising material for simultaneously performing NO_3-N removal and improving the selectivity of N_2, which provides a theoretical reference for NO_3-N remediation from wastewater.

Keywords: nitrate; nZVI/Zr-Ce-SBA-15; response surface methodology; artificial neural network combined with genetic algorithm; radial basis neural network

Citation: Zhang, R.; Liu, H.; Jiang, W.; Liu, W. Ordered Mesoporous nZVI/Zr-Ce-SBA-15 Catalysts Used for Nitrate Reduction: Synthesis, Optimization and Mechanism. *Catalysts* **2022**, *12*, 797. https://doi.org/10.3390/catal12070797

Academic Editor: Narendra Kumar

Received: 27 May 2022
Accepted: 14 July 2022
Published: 19 July 2022

1. Introduction

Excessive concentrations of nitrate (NO_3-N) entering rivers and lakes can stimulate the growth of algae, resulting in the deterioration of water quality, reduction in biodiversity and degradation of the ecosystem [1,2]. Although many countries have made efforts to reduce NO_3-N emissions to the environment, it is still one of the most serious environmental issues faced across the world [3]. In particular, its concentration in approximately 35% of well water in Tuscany in Italy exceeded 50 mg/L [4]. According to a groundwater survey in Alabama (America), NO_3-N levels in most parts of the central and northeast areas of the state were greater than 63 mg/L, and even exceeded 112 mg/L in some areas [5]. Similarly, in the vast rural and suburban areas of China, many people drink seriously polluted well water for a long time without knowing its harm [6]. NO_3-N is of lower toxicity, while it can be reduced to nitrite after entering the human body, and the toxicity of nitrite can be 11 times higher than NO_3-N [7]. The main biological effect of nitrite is to oxidize normal

hemoglobin into a type that does not have the ability to deliver oxygen, reducing the ability of hemoglobin to deliver oxygen to methemoglobin. When A concentration of methemoglobin of more than 10% of the normal hemoglobin concentration will lead to methemoglobin disease (such as Verticillium wilt). The clinical symptoms include skin cyanosis, dizziness, nausea, accelerated heartbeat, dyspnea, fatigue, abdominal pain, and diarrhea. Higher concentrations will cause asphyxia and even death [8]. Therefore, excessive NO_3-N concentrated in the water body will seriously threaten human health. Several effective measures must be taken to control and prevent NO_3-N pollution in water environments.

Hereto, the methods of removing NO_3-N from water mainly include chemical denitrification, catalytic denitrification, reverse osmosis, electrodialysis, ion exchange, biological denitrification, adsorption, etc. [9–11]. Among them, adsorption is a superior method to remove NO_3-N from wastewater due to its low cost and fast reaction [12]. In particular, nanoscale zero-valent iron (nZVI) is widely used in environmental remediation because of its superior adsorption performance and higher reduction activity. nZVI is excellent in the treatment of heavy metals and organics as well as NO_3-N in water. However, the easy agglomeration and poor antioxidation of nZVI limit its application in the field of wastewater treatment [13]. Zhou and Li [14] used nZVI and modified polyethylene carrier, a novel composite packing of tea polyphenol, to remove NO_3-N. Their results demonstrated a novel approach for the fast and eco-friendly preparation and efficient application of nZVI. Zhang et al. [15] fabricated the nZVI supported on pillared clay, which was used for NO_3-N removal. Their results showed that NO_3-N could be absolutely removed by nZVI/PILC within 120 min. This efficiency was not only much higher than that (62.3%) when using nZVI alone, but was also superior to the reduction (71.5%) seen with nZVI plus adsorption (9.19%). The end-products of NO_3-N reduction were identified as NH_4^+-N and N_2, implying that nZVI/PILC may help to cut down the total amount nitrogen in water. Obviously, it is urgent to modify nZVI to avoid easy agglomeration and poor antioxidation, and thus achieving an efficient NO_3-N removal from water.

SBA-15, as a mesoporous molecular sieve, has a high specific surface area, larger pore volume, regular pores and improved mechanical and hydrothermal stability [16]. It has attracted extensive interest in the fields of catalysis, separation, biology and nanomaterials. In particular, the short-channel SBA-15 mesoporous materials with regular morphology have potential applications in many fields. However, due to the inherent shortcomings, such as its low chemical reaction activity, its practical application range is greatly limited [17]. Traditional SBA-15 is rod-shaped or fibrous [17]. When traditional SBA-15 is used as a carrier in the fields of adsorption, separation, and catalysis, its long pores in the micron range are not conducive to the diffusion and transmission of substances into the pores. Therefore, the synthesis of mesoporous SBA-15 materials with small pores has been studied [18]. Chen et al. [19] synthesized organic functionalized short-channel plate SBA-15 with P123 as the template and trace Zr (IV) under strong acid conditions. For the adsorption of organic macromolecules, short-channel plate SBA-15 shows a better transmission capacity than traditional SBA-15. In addition, metal oxides generally exhibit excellent catalytic performances; the catalytic activity of Ce is slightly lower than that of the precious metals [20]. The cost of Ce is lower than precious metals, and it can replace precious metals as catalysts to catalyze some important reactions. Therefore, Zr-Ce-SBA-15 combined with nZVI may result in shortly ordered channels, a higher catalytic capacity, and stronger reduction ability.

Currently, several studies [20,21] have reported nZVI/SBA-15 used for environmental remediation. Tang et al. [21] successfully prepared nZVI/SBA-15 used for the effective degradation of p-nitrophenol. Their results showed that abundant ultrasmall nanoscale zero-valent iron particles were formed and well dispersed on mesoporous silica (SBA-15). A previous study [22] used short-channel hexagonal ordered mesoporous Zr-Ce-SBA-15 materials as a carrier and adopted double-solvent impregnation calcination. nZVI-confined composites in ordered mesoporous channels were synthesized through a reduction method and used to remove Trinitrotoluene. Overall, nZVI/Zr-Ce-SBA-15 may possess excellent

potential for NO_3-N removal, and unfortunately, to the best of our knowledge, these works were not reported. Therefore, the objective of the present study is to (1) fabricate the ordered mesoporous nZVI/Zr-Ce-SBA-15 composites used for NO_3-N removal, and tentatively try to improve the selectivity of N_2; (2) characterize the as-prepared nZVI/Zr-Ce-SBA-15 composites using different approaches, including X-ray diffraction (XRD), scanning electron microscopy combined with energy dispersive spectrum (SEM-EDS), N_2-sorption, high-resolution transmission electron microscope (HRTEM), and X-ray photoelectron spectroscopy (XPS); (3) optimize/predict the parameters of NO_3-N removal and nitrogen generation from simulated wastewater by nZVI/Zr-Ce-SBA-15 composites with the aid of response surface methodology (RSM), a back-propagation neural network combined with genetic algorithm (ANN-GA) and a radial basis function neural network (RBFNN).

2. Materials and Methods

2.1. Materials and Chemicals

All chemical reagents were of analytical grade, and all solutions were prepared with high-purity water (18.25 M/cm) from a Milli-Q water purification system. Triblock copolymer P123 (A.R.) was purchased from BASF Corp. (Florham Park, NJ, USA) and Tetraethyl orthosilicate (TEOS) came from ChengDu Chron Chemicals Co., Ltd. (Chengdu, China). $ZrOCl_8H_2O$, $Ce(NO_3)_3{\cdot}6H_2O$, $CH_3(CH_2)_4CH_3$ was from Sinopharm Chemical Reagent Co., Ltd. (Shanghai, China), Shanghai Qingxi Chemical Technology Co., Ltd. (Shanghai, China), and Nanjing Chemical Reagent Co., Ltd. (Nanjing, China), respectively. High-purity nitrogen was purchased from Shanghai bio gas Co., Ltd. (Shanghai, China).

2.2. Preparation of nZVI and nZVI/Zr-Ce-SBA-15

A certain amount of triblock copolymer P123 was weighed and added to 80 mL deionized water, and then heated and stirred at 35 °C, so it dissolved and formed micelles. Immediately, appropriate amounts of $ZrOCl_2{\cdot}8H_2O$, $Ce(NO_3)_3{\cdot}6H_2O$, and TEOS were put in the above micellar solution, in which the molar ratio of reactants was 0.01P123:1TEOS: $170H_2O$: $0.05ZrOCl_2{\cdot}8H_2O$: 0.05 $Ce(NO_3)_3{\cdot}6H_2O$. The mixtures were continuously stirred at 35 °C for 20 h. The formed gel was transferred into an autoclave for crystallization at 24 h at 100 °C and then cooled to room temperature. After, the produced white materials were filtered, washed, dried and finally calcined in 550 °C air atmosphere for 6 h (heating rate is 1 °C/min) to remove the template. Finally, the white powder sample is Zr-Ce-SBA-15.

nZVI/Zr-Ce-SBA-15 composites were fabricated following the method of Tang et al. [21]. Firstly, with continuous stirring, the as-prepared Zr-Ce-SBA-15 of 1.0 g was mixed with 30 mL of n-pentane. Fe(II) aqueous solution prepared by 1.112 g $FeSO_4{\cdot}7H_2O$ was gradually added into the above mixtures. The above mixture was dried at 60 °C for 12 h. Then, with continuous N_2 protection and stirring, 8 mL $NaBH_4$ solution (2 M) was added into the mixtures from the previous step, reducing Fe(II) to metallic Fe^0. The obtained materials were separated from mixtures using a magnet, washed with methanol three times, and then dried in vacuum at 50 °C for 20 h. Meanwhile, 4.0 g of $FeSO_4{\cdot}7H_2O$ was dissolved in 200 mL of methanol and deoxygenated water to fabricate nZVI. Immediately, with continuous N_2 protection and stirring, 10mL of $NaBH_4$ solution (2.1 M) was added gradually to the above solution, lasting for 30 min. The black solid was successively washed with ethanol and deionized water, and the nZVI was dried in vacuum at 50 °C for 20 h. Figure 1 shows the flow chart for preparing nZVI/Zr-Ce-SBA-15.

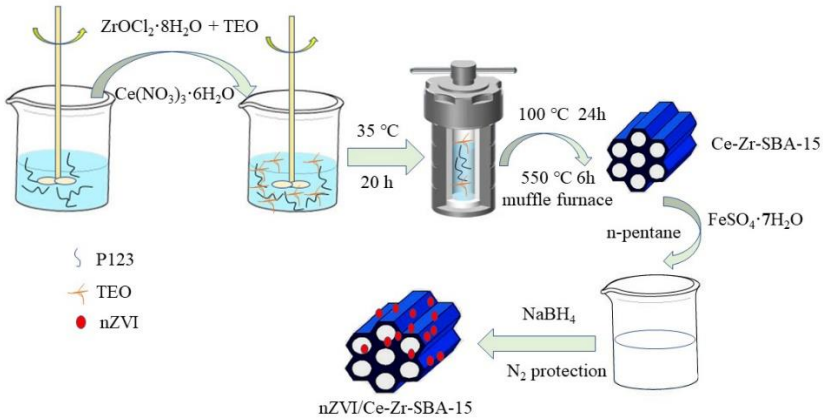

Figure 1. The flow chart for preparing nZVI/Zr-Ce-SBA-15.

2.3. Characterizations

The morphology of the samples was characterized by TEM (JEM-2100, Akishima, Tokyo, Japan) and SEM (Jsm-6490lv, JEOL, Tokyo, Japan). XRD (RIGAKUD/max 2500) was used to test the crystal structure of the sample with a test voltage of 40 kV, current of 20 mA, scanning rate of 2 (°)/min, and Cu target Kal radiation line (λ = 0.15405 nm). The N_2 adsorption–desorption isotherm, specific surface area and pore size distribution of the samples were measured by a 3Flex specific surface area pore analyzer (USA). The binding energy was tested by XPS (Thermoescalab 250Xi). The monochromatic alka hv = 1486.6 EV, power was 150 W, 500 um beam spots were used, and the binding energy was calibrated with C1s 284.8 eV. Nitrate and nitrite concentrations in the solution were determined by sulfamate spectrophotometry and N-(1-naphthyl)-ethylenediamine photometry, respectively. Nanoreagent spectrophotometry was used to test ammonia concentration in the solution. Fe^{2+} contents were determined by o-phenanthroline spectrophotometry (APHA, 2005). Total nitrogen (TN) was equal to the sum of NH_4^+-N, NO_3-N, and NO_2-N.

2.4. Batch Experiments for NO_3-N Removal Using nZVI/Zr-Ce-SBA-15 Composites

The stock solution of NO_3-N was prepared from $NaNO_3$ (analytical purity). The stock solution of 1000 mg /L NO_3-N was gradually diluted to 40, 60, and 80 mg/L. A total of 0.15 g of nZVI/Zr-Ce-SBA-15 composites was placed in a 250 mL glass bottles, and 50 mL of NO_3-N stock solution at 40, 60, and 80 mg/L concentrations (actual concentrations of 39.17, 60.82, and 79.65 mg/L) was, respectively, added into the above conical flask with a microinjector. The glass bottle was sealed and put in the thermostat water bath to remove NO_3-N. The samples were collected at certain intervals with a needle tube and immediately filtered with a 0.22 μm filter membrane. Immediately, the samples were analyzed by assessing the changes in NO_3-N, N_2 and NO_2-N, NH_4^+-N contents in the solution over time, thus obtaining the adsorption capabilities (q_e), removal efficiency (P), NO_2-N productivity ($S_{NO2\text{-}N}$), N_2 productivity (S_{N2}) and NH_4^+-N productivity ($S_{NH_4^+\text{-}N}$) (Equations (1)–(5)). The glass bottle and reaction solution were deoxidized before the reaction. The pH of the solution was adjusted by H_2SO_4 and $NaHCO_3$.

$$q_e = \frac{C_0 - C_{NO_3-N}}{m} \times v \quad (1)$$

$$P = \frac{C_0 - C_{NO_3-N}}{C_0} \times 100\% \quad (2)$$

$$S_{NH_4^+-N} = \frac{C_{NH_4^+-N}}{C_0 - C_{NO_3-N}} \quad (3)$$

$$S_{NO_2-N} = \frac{C_{NO_2-N}}{C_0 - C_{NO_3-N}} \quad (4)$$

$$S_{N_2} = \frac{C_0 - C_{NO_3-N} - C_{NO_2-N} - C_{NH_4^+-N}}{C_0 - C_{NO_3-N}} \quad (5)$$

where C_0 is the concentration of NO_3-N in the solution before adsorption, mg/L; $C_{NO3\text{-}N}$, C_{NO_2-N}, and $C_{NH_4^+-N}$ are the concentrations of NO_3-N, NO_2-N and NH_4^+-N in the solution after adsorption, mg/L; m is the mass of nZVI/Zr-Ce-SBA-15, g; q_e is the equilibrium adsorption quality of nZVI/Zr-Ce-SBA-15, mg/g; P is the adsorption efficiency; S_{NO_2-N}, S_{N_2}, and $S_{NH_4^+-N}$ represent the productivity of NO_2-N, N_2 and NH_4^+-N. The following steps were used for batch experiments using optimal nZVI/Zr-Ce-SBA-15. (1) Isothermal adsorption: the initial concentration gradients of NO_3-N were set to 20, 40, 60, 80 and 100 mg/L. (2) Adsorption kinetics: the adsorption times of NO_3-N were set to 1, 5, 10, 20, 30, 60, 120, and 180 min; other settings are the same (nZVI/Zr-Ce-SBA-15 = 0.15 g; initial pH = 4; temperature = 25 °C).

2.5. Modeling Methods of RSM, ANN-GA and RBFNN

The second-order model designed by Box–Behenken design (BBD) was used to study the relationship between response and variable values (Table 1). The selected variables are initial pH (x_1), contact time (x_2), temperature (x_3) and initial NO_3-N concentration (x_4). The response values are the removal rate of NO_3-N (y). The second-order model of BBD is shown in Equation (6):

$$y = \beta_0 + \sum_{i=1}^{k} \beta_i x_i + \sum_{i=1}^{k} \beta_{ii} (x_i)^2 + \sum_{i=1}^{k-1} \sum_{ij}^{k} \beta_{ij} x_i x_j + \varepsilon \quad (6)$$

where β_0, β_i, β_{ii} and β_{ij} are the intercept, primary term coefficient, secondary term coefficient and interaction coefficient, respectively, and ε is the test residual. The ANN-GA design was followed according to Xiang et al. [23] and ran in MATLAB 2016a. The modeling process of RBFNN is referred with [24,25].

Table 1. Parameter level of BBD experimental design.

Code	Parameters	Maximum	Middle	Minimum
x_1	Initial pH	5	4	3
x_2	Contact time (min)	70	60	50
x_3	Temperature (°C)	25	20	15
x_4	Initial NO_3-N concentration	80	60	40

3. Results and Discussion

3.1. Characterization of Zr-Ce-SBA-15 and nZVI/Zr-Ce-SBA-15 Composites

Figure 2 exhibits that the diffraction peak of nZVI is 44.88°, and its corresponding crystal plane is (100). After NO_3-N adsorption onto pure nZVI, the diffraction peak of nZVI was basically unchanged. A strong and broad-band satellite peak of Zr-Ce-SBA, nZVI/Zr-Ce-SBA, nZVI/Zr-Ce-SBA@NO_3-N composites was found in the range of 2θ = 20–30° due to the amorphous silica walls of mesoporous material [26]. In addition, a crystal plane (100) at 44.88° was also found in nZVI/Zr-Ce-SBA-15 and nZVI/Zr-Ce-SBA@NO_3-N composites, implying that nZVI was successfully supported onto Zr-Ce-SBA-15 and its valence state is α-Fe^0 [26].

The silica material exhibits two asymmetric stretching vibrational modes of siloxane moieties (–Si–O–Si–) at 1079.9 cm^{-1} and 814.2 cm^{-1}, and bending vibrational modes at 450.9 cm^{-1} [27,28] (Figure 3). The characteristic band of the hydroxyl group was found at 3455.8 cm^{-1} for the H_2O molecule, and the intense absorption band at 1637.2 cm^{-1} for the five materials is attributed to carbonyl groups, exhibiting that they are of the massive oxygen-containing unsaturated group. The peaks at 548 cm^{-1} and 621 cm^{-1} corresponding to Fe-O stretches of iron oxide were observed for the nZVI/Zr-Ce-SBA-15 and nZVI/Zr-

Ce-SBA-15 compositions, suggesting that nZVI was adsorbed onto Zr-Ce-SBA-15 and the oxidation occurred on the surface of nZVI particles. The peak for the Fe-O bond shifted to 636 cm^{-1} and 540 cm^{-1} after the adsorption of NO_3-N, indicating the transformation of different phases of iron oxides during aging. The characteristic band of nZVI and nZVI/Zr-Ce-SBA-15 at 1383.7 cm^{-1} is obviously enhanced after the adsorption of NO_3-N, which may be the characteristic nitro peak.

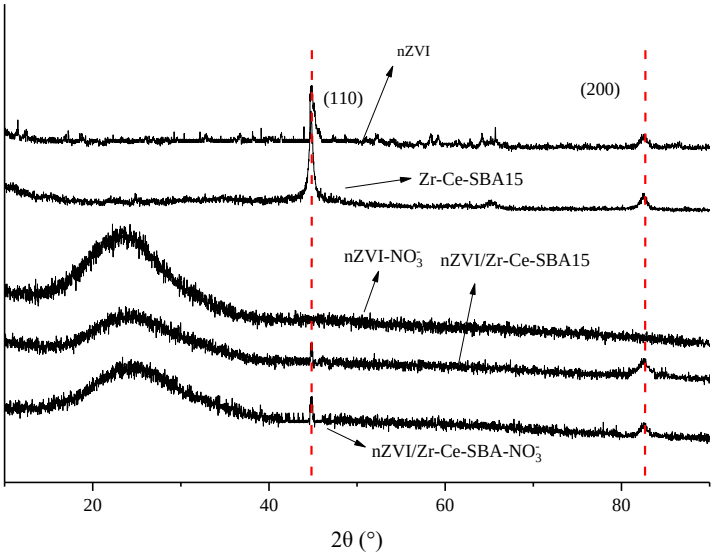

Figure 2. XRD characterization of nZVI/Zr-Ce-SBA-15 composites.

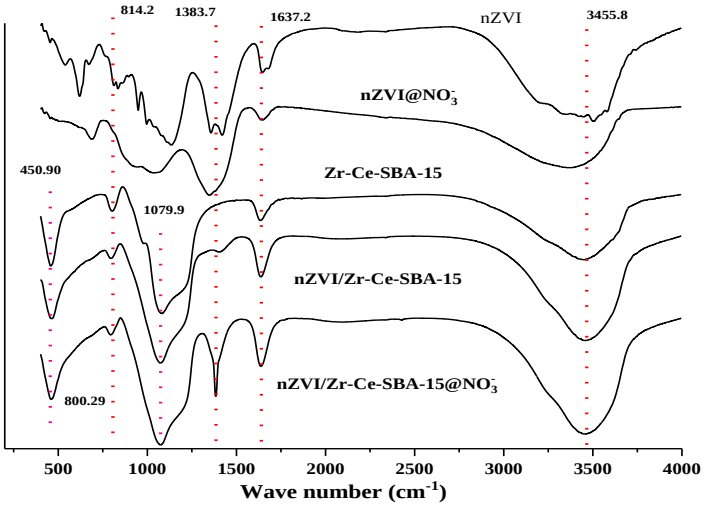

Figure 3. FTIR characterization of nZVI/Zr−Ce−SBA−15 composites.

Zr-Ce-SBA-15 is a hexagonal plate structure (Figure 4), with uniform size, a radial length of 1.5 μm and an axial length of 0.5 μm. There was no obvious change in the morphology of the two mesoporous materials after loading nZVI, indicating that the loading of nZVI does not damage the structure of mesoporous materials [29]. According to analysis of SEM-EDS, the element ratio of Zr-Ce-SBA-15 is 22.04% (C), 58.1% (O), 1.08% (N), 2.08% (Na), 13.79% (Si), 2.25% (Fe) and 0.66% (Zr). Apparently, the corresponding Si and Zr maps evidenced bright spots corresponding to the selected area and illustrated a homogeneous distribution of these elements in the field of view of the cross-section (Figure S1a,b).

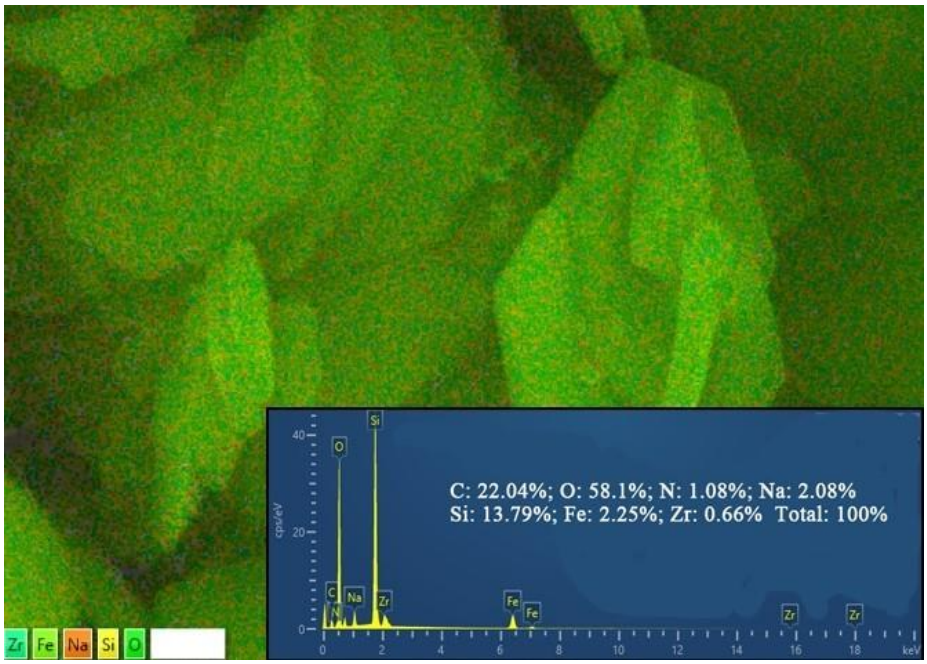

Figure 4. SEM characterization of nZVI/Zr-Ce-SBA-15 composites.

Figure 5a shows that Zr-Ce-SBA-15 has regular black-and-white stripes, with the hole wall and the mesoporous channel being black and white, respectively. The channel and the long axis direction are mutually parallel in the material. Figure 5b also exhibits that the mesoporous materials have long-range-ordered pores and a uniform pore size, which is consistent with the results of small-angle XRD in the previously published literature [22]. The channel direction of nZVI/Zr-Ce-SBA-15 is perpendicular to the hexagonal plate and parallel to the axial direction of the hexagonal plate. Figure 5b demonstrates that the composite material still has neat black-and-white stripes, indicating that the mesoporous structure is not damaged after the loading of nZVI particles; meanwhile, the material still maintains a certain order. There are a large number of black particles on the surface of the composite, which are nZVI particles on the carrier. These particles are of small size and evenly distributed on the carrier without obvious agglomeration. No nZVI particles dispersed outside were found in nZVI/Zr-Ce-SBA-15 composites, indicating that most of the nZVI particles in the composites synthesized entered the pores. The results further show that the method used in the present study can make it easier for metal particles to enter the carrier channel, limiting the chance of them remaining in the channel, and avoiding the growth and agglomeration of nZVI particles [30].

According to IUPAC, the curve of the nZVI/Zr-Ce-SBA-15 composites belongs to the type IV isotherm and had obvious pore condensation, indicating that the synthesized materials had a mesoporous structure (Figure S2). The existence of H1-type adsorption shows that the sample had a columnar pore structure; these characteristics are unique to mesoporous nZVI /Zr-Ce-SBA-15 materials [30]. In addition, compared to nZVI and Zr-Ce-SBA-15, the adsorption capacity of N_2 increased significantly. The specific surface areas of nZVI and nZVI/Zr-Ce-SBA-15 were 292 and 790 cm^2/g, respectively, and generally, the larger the specific surface areas of mesoporous materials, the higher the adsorption capabilities of pollutants are [30].

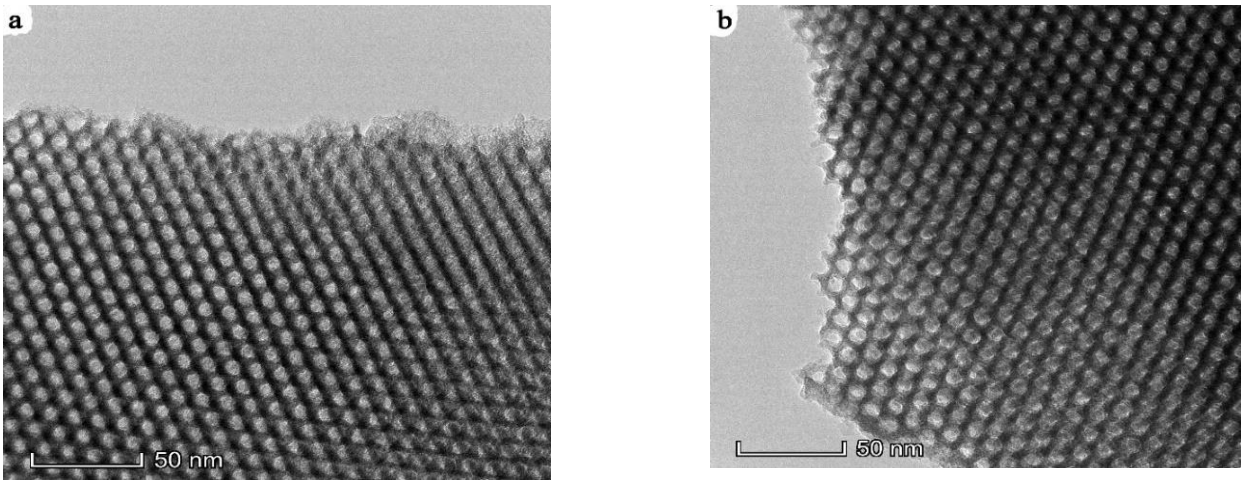

Figure 5. HRTEM characterization of Zr-Ce-SBA-15 composites (**a**) and nZVI/Zr-Ce-SBA-15 composites (**b**).

Figure 6 exhibits nZVI before and after loading onto Zr-Ce-SBA-15 composites. A weak peak for C1s and Si2p was found in the Zr-Ce-SBA-15 and nZVI/Zr-Ce-SBA-15 composites. Among them, the carbon that appears in the two samples results from the internal standard used to calibrate the binding energy of the other elements [31]. The existence of O1s confirmed that the two materials were of the massive oxygen-containing unsaturated groups, which are mainly from P123 and TEO. Obviously, before the nZVI loading onto Zr-Ce-SBA-15 composites, no peak was found in the range from 700 eV to 740 eV (Figure S3a). Further, after the nZVI loading onto Zr-Ce-SBA-15 composites, Fe(0), Fe(II) and Fe(III) were found at 710.5 eV, 711.8 eV, and 713.6 eV, suggesting that nZVI was loaded onto Zr-Ce-SBA-15 composites (Figure S3b). However, it was also found that nZVI had begun to be oxidized at this point.

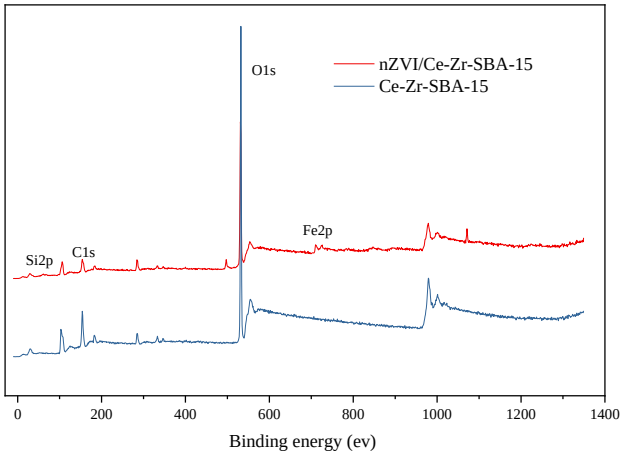

Figure 6. XPS characterization of Zr-Ce-SBA-15 and nZVI/Zr-Ce-SBA-15 composites.

3.2. Optimization of the NO_3-N Removal from Simulated Wastewater by RSM

Table 2 exhibits 29 groups of treatment designs using BBD. The experimental results are fitted by a quadratic polynomial, and the NO_3-N removal rate was selected as the response value (Equation (7)):

$$y = 87.18 + 4.82x_1 + 2.96x_2 - 1.45x_3 + 1.76x_4 - 1.81x_1x_2 + 2.17x_1x_3 + 6.61x_1x_4 + 4.89x_2x_3 - 1.01x_2x_4 - 1.22x_3x_4 - 8.52x_1^2 - 0.90x_1^2 - 2.22x_3^2 - 0.34x_4^2 \quad (7)$$

where y is the removal rate of NO_3-N, %; x_1, x_2, x_3 and x_4 are the coded values of the initial pH, contact time, temperature, and initial NO_3-N concentration, respectively. The positive

sign (+) before the coefficient suggests a synergy between factors, and the negative sign (−) indicates the opposite relationship between factors. The absolute value of the coefficient can judge the effects of various factors on the adsorption effect of NO_3-N. Obviously, the order of the impact factors was initial pH > contact time > initial NO_3-N concentration > temperature. Yang et al. [32] optimized the nitrite-removal process from pickled meat by garlic by RSM. They found that the effect of extraction temperature on garlic clearance was the most significant, which showed that the surface was steep, followed by the amount of extraction solution, pH value of reaction solution and reaction time, and the relative effect of extraction time was the least. Rahdar et al. [33] used RSM to optimize the removal of NO_3-N by adsorption onto copper oxide nanoparticles. Their results suggest that the order of influence factors was NO_3-N concentration > initial pH > CuO-NPS dose > contact time. This is not inconsistent with this study, which shows that NO_3-N and nZVI were perhaps sensitive to pH in solutions.

Table 2. BBD test scheme and results.

Order	Contact Time (min)	Temperature (°C)	Initial NO_3-N Concentration(mg/L)	Initial pH	NO_3-N Removal Efficiency (%)
1	50	20	60	3	65.03
2	60	25	60	3	63.48
3	60	15	60	3	73.41
4	60	20	80	3	57.61
5	70	20	60	3	76.18
6	60	20	40	3	82.91
7	70	25	60	4	88.17
8	60	20	60	4	87.83
9	60	20	60	4	90.58
10	60	15	80	4	86.31
11	50	15	60	4	87.9
12	70	20	40	4	93.72
13	70	20	80	4	83.05
14	60	25	80	4	80.16
15	60	20	60	4	84.24
16	70	15	60	4	80.99
17	50	25	60	4	75.52
18	60	15	40	4	83.28
19	60	20	60	4	85.97
20	60	25	40	4	83.62
21	50	20	40	4	85.66
22	60	20	60	4	84.14
23	50	20	80	4	80.38
24	60	15	60	5	85.14
25	50	20	60	5	80.94
26	60	20	40	5	79.06
27	60	20	80	5	88.99
28	70	20	60	5	84.84
29	60	25	60	5	83.87

F and p values represent the significance of the developed model. According to the results of analysis of variance (Table 3), the adaptability of the developed model with NO_3-N removal is very significant ($F = 1739.25$, $p < 0.0001$). The mismatch term is less than 0.05, indicating that the model fitting is not significant, which also reflects the significant relationship between the factors described in the model and the response value. The determination coefficient ($R^2 - R^2adj = 0.0528 < 0.2$) is 0.9821, indicating that the experimental and predicted values are closed (Figure S4). The coefficient of variation (3.23%) is less than 10% and the precision of the analysis (17.28) is greater than 4, indicating that the reliability and accuracy of the model are high. Precision is the ratio of effective signal to noise,

which is considered reasonable when its value is greater than 4. Overall, the quadratic models established by BBD can better fit the process of the NO_3-N removal using nZVI/Zr-Ce-SBA-15 composites, which can be used to optimize the experimental conditions.

Table 3. Response surface variance analysis results.

Source	Sum of Squares	Degree of Freedom	Mean Square	F Value	*p* Value	Source
Model	1739.25	14	124.23	17.95	<0.0001	significant
x	234.42	1	234.42	33.86	<0.0001	
x_1	88.75	1	88.75	12.82	0.003	
x_2	21.11	1	21.11	3.05	0.1027	
x_3	45	1	45	6.5	0.0231	
x_4	13.14	1	13.14	1.9	0.1899	
x_1x_2	18.75	1	18.75	2.71	0.1221	
x_1x_3	310.29	1	310.29	44.82	<0.0001	
x_1x_4	95.65	1	95.65	13.82	0.0023	
x_2x_3	7.26	1	7.26	1.05	0.3231	
x_2x_4	10.53	1	10.53	1.52	0.2378	
x_3x_4	470.78	1	470.78	68.01	<0.0001	
x_1^2	5.3	1	5.3	0.7663	0.3961	
x_2^2	31.98	1	31.98	4.62	0.0496	
x_3^2	2.4	1	2.4	0.3465	0.5655	
x_2^4	96.91	14	6.92			
Lack of Fit	67.55	10	6.76	0.9204	0.5862	not significant
Pure Error	29.36	4	7.34			
Cor Total	1836.16	28				

R^2 = 0.9472; Adj.R^2 value = 0.8944; Pre.R^2 value = 0.7631; adequate precision = 17.28; coefficient of variation = 3.23%.

According to the analysis of the quadratic fitting model, the optimized experimental conditions within the experimental range of this study are 24.35 °C (temperature), 69.98 min (contact time), 3.79 (initial pH), and 40.58 mg/L (initial NO_3-N concentration). In order to facilitate practical operation and analysis, the conditions can be adjusted to 24.4 °C, 70.00 min, pH = 3.8 and 40.6 mg/L, respectively, and the theoretical removal capacity under these conditions is 93.84%. The experiment was carried out under the above conditions and three groups were set up in parallel, and the experimental results were taken as the average. Finally, the optimized actual NO_3-N removal rate was 92.07%, and the absolute error between them was 1.77%. There are few studies on the removal of NO_3-N by RSM, and NO_2-N was therefore used for discussion in the present study. Rahdar et al. [33] utilized RSM to optimize NO_3-N removal with factors (input): initial NO_3-N concentration (20, 45, and 70 mg/L), CuO single-bond NP concentration (0.03, 0.06, and 0.08 g/L), pH (3, 7, and 11) and reaction time (40, 80, v120 min). The optimum conditions found were 70 mg/L for nanoparticles dose, 0.08 g/L for NO_3-N concentration, Ph = 3, and 120 min contact time. The above studies confirmed RSM as a reliable tool, and our results are not exactly the same as the two references, which may be due to the different subjects. Figure 7 demonstrates that the 3D response surface analysis concerning the interaction between the four factors affected the NO_3-N removal efficiency. The steeper the 3D surface, the greater the interaction between the two factors.

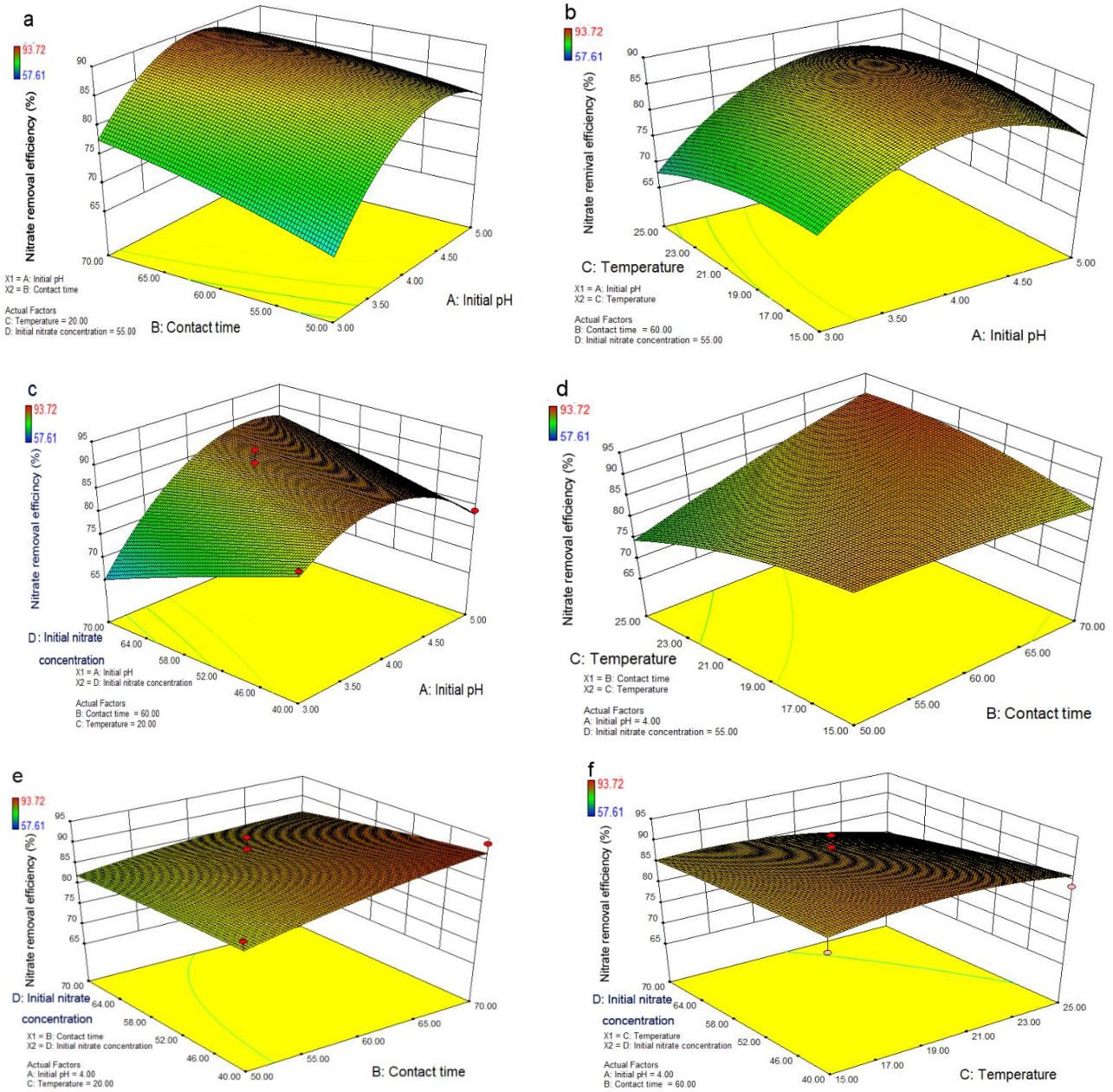

Figure 7. 3D response surface (**a**) of the effects of contact time and initial pH on removal efficiencies; 3D response surface (**b**) of the effects of temperature and initial pH on removal efficiencies; 3D response surface (**c**) of the effects of initial NO_3-N concentration and initial pH on removal efficiencies; 3D response surface (**d**) of the effects of temperature and contact time on removal efficiencies; 3D response surface (**e**) of the effects of initial NO_3-N concentration and contact time on removal efficiencies; 3D response surface (**f**) of the effects of initial NO_3-N concentration and temperature on removal efficiencies.

3.3. Optimization of the NO_3-N Removal from Simulated Wastewater by ANN-GA and RBF

The 29-group dataset designed by BBD in RSM was used as the source of the sample set. From 29 groups of BBD, 24 groups were randomly selected as the input vector of the training sample set, and the remaining 5 groups were used as the input vector of the prediction sample set. The error value between the actual and target outputs of the training sample in the neural network reflects the network training accuracy. A smaller value can mean that the number of network training steps is too large and time consuming. The higher error value will render the network incapable of evaluating the nonlinear

mapping relationship accurately and cannot realize the simulation and prediction function. Therefore, referring to the work of Xiang et al. [23], the parameters of the developed ANN model are as the follows: epoch—2000; learning rate—0.1; goal—1×10^{-5}; and momentum factor—0.9 (Figure S5a). Most processing methods transform the original test data into 0 to 1 in a specific way to improve the network training effect and network simulation ability. In this study, to eliminate the numerical difference between the parameters of the input and the layers, the test data were first normalized using the mapminmax function covered by the Matlab toolbox before the network operation. The model developed by the ANN is a 'black box model', and its R^2 value is 0.99159, indicating that the experimental and predicted values of the model are highly consistent (Figure S6a) A lower or higher number of neurons in the hidden layer may lead to insufficient fitting or overfitting for the developed ANN model, respectively, reducing the prediction ability of model. The present study selected six neurons used in the hidden layer based on the lowest MSE value (Figure S6b).

GA was used to optimize the established BP neural network model and its basic parameters of GA by referring to Xiang et al. [23] (population size = 20; cross probability = 0.8; mutation probability = 0.01; genetic probability = 0.9; maxgen = 500). The network model is called fitness function. In the initial stage, the population search characteristic of GA has an obvious role, showing that the NO_3-N removal rate of the selected individuals has increased sharply. Then, GA was used to conduct a stable cross operation, making it so that the NO_3-N removal rate did not change. The optimization process of GA was used to carry out a selection operation, and the NO_3-N removal rate of the selected individual had a small range of positive changes, approaching the target step by step. The curve change process in Figure 8 shows that the NO_3-N removal rate converges at 93.45% at the 50th iterations. After a series of cyclic iterative operations, including crossover, selection, mutation, crossover, selection, the program of GA was terminated and obtained the highest NO_3-N removal rate with its optimization evolution iterations reaching 105 generations. The removal rate of NO_3-N by nZVI/Zr-Ce-SBA-15 composites reached 95.71% under the optimal parameters: initial pH = 4.89; contact time = 62.27 min; initial NO_3-N concentration = 74.84 mg/L; temperature = 24.77. Based on the above parameters, the experimental removal rate of NO_3-N is 94.64%, and the absolute error of removal efficiencies between the predicted and actual values is merely 1.07%. RBFNN is superior to the BP neural network in terms of approximation ability, classification ability and learning speed. It has a simple structure, is simple the train, and has a fast learning convergence speed, which can approximate any nonlinear function and overcome the problem of a local minimum. The reason for this is that its parameter initialization has a distinctive method, not a random initialization [34]. The parameters of the developed RBFNN model were set as the follows: spread = 0.8; err goal = 1×10^{-10}. After obtaining the predicted results of ANN-GA, the developed RBFNN model was used to verify the accuracy of them again. The training process was terminated after the MSE value reached 0.0226085 (Figure S5b), and the predicted and actual values were very consistent, confirming the reliability of the ANN-GA model (Figure S7). Cai et al. [35] reported that the prediction of the performance of simultaneous anaerobic sulfide and NO_3-N removal in an upflow anaerobic sludge bed reactor through an ANN. Their results showed that the ANN model predicted the simultaneous sulfide and NO_3-N removal process accurately. Lee et al. [36] studied NO_3-N sorption onto quaternary ammonium-functionalized poly(amidoamine) dendrimer, generation 2.0. Based on a pH experiment, these materials maintained a relatively stable NO_3-N sorption capacity in the pH range from 2 to 10. They also suggested that the developed ANN model (R^2 = 0.872) predicted more accurately than the RSM model (R^2 = 0.790) for the additional multi-parameter experimental data. Multi-parameter experiments and modeling for NO_3-N sorption were conducted on quaternary ammonium-functionalized poly(amidoamine) dendrimers in aqueous solutions. Due to its nonlinear fitting, the performance of ANN is obviously better than that of RSM. Liu et al. [37] introduced two widely used ANN models, the basic theories of BP and RBF neural networks, and expounded the learning process of the two algorithms from a mathematical point of view. The simulation results show that

the generalization ability of RBF is better than the BP network in many aspects, but the structure of BP network is simpler than RBF network when solving the problem with the same accuracy requirements.

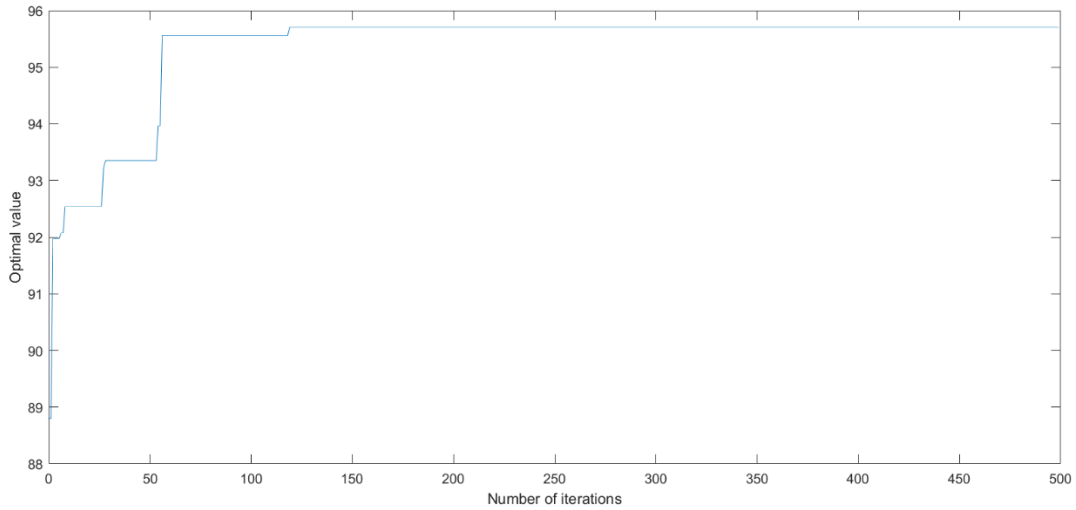

Figure 8. The predicted optimal NO_3-N removal efficiency by ANN-GA model.

3.4. Kinetic Model, Isothermal Adsorption and Thermodynamic Parameters for NO_3-N Removal

The kinetics process is mainly used to describe the rate of solute adsorption by adsorbent. The adsorption mechanism can be inferred by fitting the data to the kinetic model. The experimental data were fitted by two kinetic models (Equations (8) and (9)) [38].

$$\ln(q_e - q_t) = \ln q_e - k_1 t \quad (8)$$

$$\frac{t}{q_t} = \frac{1}{k_2 {q_e}^2} + \frac{t}{q_e} \quad (9)$$

where q_e and q_t are the adsorption capacity (mg/g) at equilibrium and time t, respectively; k_1 (1/min) is the rate constant of the pseudo-first-order kinetic model; k_2 is the rate constant for the pseudo-second-order kinetic model (g/mg·min^{-1}).

The capacities of NO_3-N adsorption onto nZVI/Zr-Ce-SBA-15 composites are shown in Figure 9a. The adsorption process with an initial NO_3-N concentration of 60 mg/L is divided into three stages, including rapid adsorption in the first 50 min, slow adsorption in the following 60 min and final apparent equilibrium adsorption. This is mainly because there are many adsorption sites on nZVI/Zr-Ce-SBA-15 composites in the initial stage. With the continuous reaction, the adsorption sites gradually decrease and reach the saturation state. The slow adsorption for 60 min may be because, with the continuous reaction, NO_3-N further diffuses into the internal pores of nZVI/Zr-Ce-SBA-15 composites and reacts with the active sites on the inner surface. A smaller internal pore size leads to difficult diffusion, making that the reaction slowed down. Compared with the pseudo first-order kinetic model, the pseudo second-order kinetic model can better fit the adsorption process ($R^2 > 0.99$), and its adsorption capacity (43.7) was nearer to the experimental value (42.6), indicating that the adsorption process was mainly controlled by chemical adsorption (Figure 9b). Zhao et al. [39] used green tea extract as a reducing agent to synthesize a nanoscale zero-valent iron–nickel bimetallic to remove NO_3-N from groundwater. The kinetic study showed that, under the optimum conditions, the removal process of NO_3-N by this material conforms to the pseudo-second-order adsorption kinetic model, which was dominated by adsorption and accompanied by the reduction reaction. Wang et al. [40] used ZVI supported on biochar composites to remove NO_3-N from groundwater. Their results demonstrated that the removal NO_3-N in water by these materials can meet the pseudo-first-order reaction only when the mass of the composite and pollutant is relatively

large. When the second-order reaction is used to simulate the reduction reaction, the reaction rate decreases obviously. Therefore, the reaction process cannot be described by the reaction order alone.

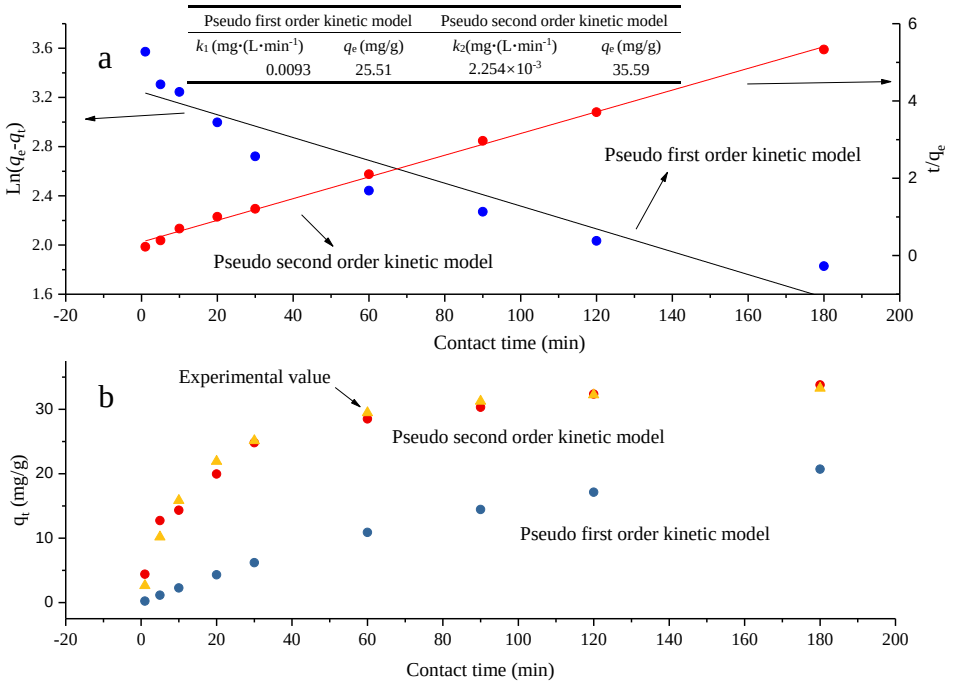

Figure 9. Comparison of pseudo-first and second-order kinetic models (**a**) and the capacities of NO_3-N adsorption onto nZVI/Zr−Ce−SBA−15 composites (**b**) (nZVI/nZVI/Zr−Ce−SBA−15 = 0.15 g; contact time = 1−180 min; initial NO_3-N concentration = 60 mg/L and initial pH = 4; temperature = 25 °C).

nZVI/Zr-Ce-SBA-15 was simultaneously adsorbed and catalyzed in the process of NO_3-N removal. Therefore, isothermal adsorption models were not suitable to describe the adsorption behavior of nZVI/Zr-Ce-SBA-15. The present study investigated the relationship between the equilibrium concentration of NO_3-N in the solution and the adsorption capacity of Zr-Ce-SBA-15 using isothermal adsorption models, and thus indirectly reflecting the adsorption capacity of NO_3-N on nZVI/Zr-Ce-SBA-15. The results show that the adsorption capacity increases with increasing NO_3-N in the solution. The adsorption capacity was not unchanged when the NO_3-N concentration in the solution reached a certain value. This may be because, with the increase in NO_3-N concentration, the adsorption sites on the surface of nZVI/Zr-Ce-SBA-15 were gradually occupied by NO_3-N under the constant doses of the adsorbents. The Langmuir and Freundlich isothermal adsorption models are as follows (Equations (10) and (11)) [41]:

$$\frac{C_e}{q_e} = \frac{1}{K_L q_{max}} + \frac{C_e}{q_{max}} \quad (10)$$

$$Lnq_e = LnK_F + \frac{1}{n} LnC_e \quad (11)$$

where C_e is the equilibrium concentration of NO_3-N in solution (mg/L), q_e is the amount of NO_3-N adsorbed (mg/g), q_{max} is q_e for a complete monolayer (maximum adsorption capacity) (mg/g) and K_L is the adsorption equilibrium constant (L/mg).

Figure 10a shows that the fitting correlation coefficient (R^2) of Langmuir and Freundlich isothermal adsorption models of NO_3-N adsorption on Zr-Ce-SBA-15 composites in simulated wastewater is greater than 0.900, indicating that their models can be better used to describe the adsorption process. A Langmuir adsorption isothermal model assumes that the adsorbent surface is uniform, the adsorption energy is the same everywhere,

and the adsorption of the adsorbent to adsorbate belongs to monolayer adsorption [42]. Compared with the Freundlich model, the Langmuir model has a higher fitting correlation coefficient for the process of NO_3-N adsorption, implying that the NO_3-N adsorption onto Zr-Ce-SBA-15 is followed more closely by the Langmuir model and belongs to monolayer adsorption (Figure 10b). The calculated R_L value is between 0 and 1, indicating that the adsorption process is preferential adsorption. According to the Langmuir model, the maximum adsorption capacity of NO_3-N in simulated wastewater by Zr-Ce-SBA-15 composites is 45.25 mg/g, which is more than that of most adsorbents (Table 4), indirectly confirming that the maximum removal capability of nZVI/Zr-Ce-SBA-15 was higher than 45.24 mg/g, Figure 10a. The n value in the Freundlich model can be used as an indicator of the adsorption of NO_3-N by Zr-Ce-SBA-15 composites. The smaller the n value is, the greater the adsorption capacity is, and the larger the K_F value is, the greater the adsorption capacity is. Meng et al. [42] utilized the in situ growth synthesis of a CNTs@AC hybrid material for efficient nitrate–nitrogen adsorption. The isothermal analysis shows that NO_3-N adsorption is made up of multiple processes with a maximum adsorption capacity of 27.07 $mg \cdot g^{-1}$. He et al. [43] studied the absorption characteristics of bamboo charcoal for NO_3-N. The Langmuir fitting results showed that K_L decreased linearly with increasing temperature, and the increase in temperature was not conducive to the adsorption of NO_3-N by bamboo charcoal. The pH value also affected the adsorption effect. When the pH value is 2.0, the adsorption effect of bamboo charcoal toward NO_3-N is at its best.

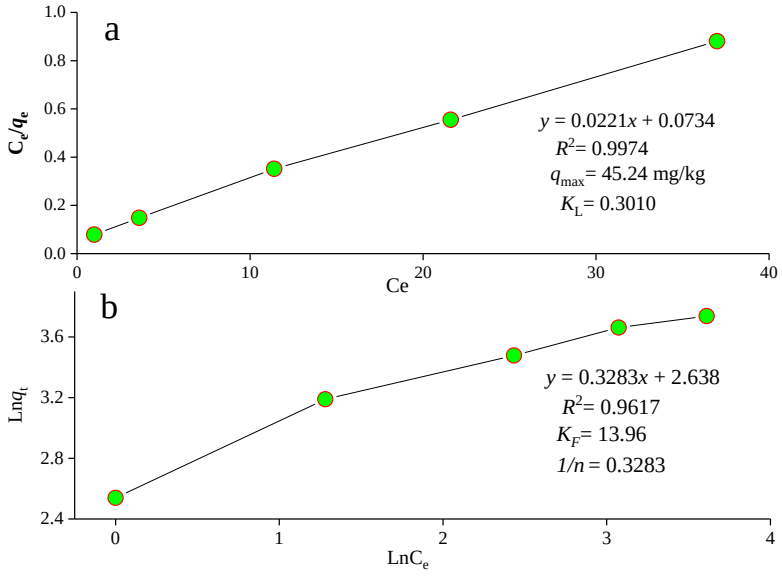

Figure 10. The fitting processes the Langmuir (**a**) and Freundlich (**b**) isothermal adsorption models (Zr-Ce-SBA-15 = 0.15 g; contact time = 180 min; temperature = 25 °C; initial pH = 4).

Adsorption thermodynamics are an important factor for the adsorption mechanism. The parameters, Gibbs-free energy change (ΔG^0), enthalpy change (ΔH^0) and entropy change (ΔS^0) are used to describe the effect of temperature on the adsorption equilibrium. ΔG^0 (J/mol) can judge the spontaneity of the adsorption reaction. The ΔH^0 (kJ/mol) can judge whether the adsorption reaction is an endothermic process or an exothermic process. The ΔS^0 (J/mol·K) represents the change of the degree of freedom of the system. Their calculated mean is found through the following equations, Equations (12)–(14) [23]:

$$\ln K_D = \frac{\Delta S^0}{R} - \frac{\Delta H^0}{RT} \quad (12)$$

$$K_D = \frac{C_0}{C_e} \quad (13)$$

$$\Delta G^0 = \Delta H^0 - T\Delta S^0 \quad (14)$$

where ΔH^0 is the standard enthalpy change (kJ/mol) and ΔS^0 is the standard entropy change ($kJ \cdot mol^{-1} \cdot K^{-1}$). The values of ΔH^0 and ΔS^0 can be obtained from the slope and intercept of a plot of lnK_0 against 1/T. ΔG^0 is the standard free energy change (kJ/mol), T is the temperature (K) and R is the gas constant (8.314 $J \cdot mol^{-1} \cdot K^{-1}$).

Table 4. Comparing the parameters of Langmuir and Freundlich isothermal adsorption models and the maximum adsorption capabilities with those of other studies [44–46].

Materials	Initial NO_3^--N Concentration (mg/L)	q_{max} (mg/g)/Removal Efficiency (%)
Trimethyl quaternary ammonium functionalized SBA-15 (C1Q-SBA1)	10–1000	89.4
Dimethylbutyl quaternary ammonium functionalized SBA-15 (C4Q-SBA1)	10–1000	129.9
Dimethyloctyl quaternary ammonium functionalized SBA-15 (C8Q-SBA1)	10–1000	136.4
Dimethyldodecyl quaternary ammonium functionalized SBA-15 (C12Q-SBA1)	10–1000	71.9
Dimethyloctadecyl quaternary ammonium functionalized SBA-15 (C18Q-SBA1)	10–1000	30.7
Propyl-ammonium SBA-15 G	100–700	55.24
Propyl-ammonium SBA-15 C	100–700	45.66
Propyl-N,N,N-trimethylammonium functionalized SBA-15 G	100–700	62.50
Propyl-N,N,N-trimethylammonium functionalized SBA-15 C	100–700	38.75
Fe-SBA-15	7.5 (15 min)	67.3%
Fe-SBA-15	12.5 (min)	50%
Fe-SBA-15	20 (min)	46.3%
Fe-SBA-15	30 (min)	43.3%
BC-Fe	20–1000 (24 h)	51.19
Zr-Ce-SBA-15	60	45.24 (In this study)

Figure S8 shows that the process of NO_3-N adsorption onto nZVI/Zr-Ce-SBA-15 composites is spontaneous. With the increase in temperature, ΔG^0 gradually decreased and the adsorption spontaneity gradually increased, indicating that the increase in temperature is more conducive to adsorption. Generally, when the ΔH^0 is less than 40 kJ/mol, adsorption is controlled by van der Waals' forces and is due to to physical adsorption. When 50 kJ/mol < ΔH^0 < 200 kJ/mol, the adsorption is controlled by chemical bonds and is due to physical adsorption [47]. The adsorption of nZVI/Zr-Ce-SBA-15 onto NO_3-N is mainly chemical adsorption, which is also in good agreement with the results of pseudo-second-order kinetic fitting. This may be due to the interaction between a small amount of organic functional groups on nZVI/Zr-Ce-SBA-15 composites or nZVI and NO_3-N. In addition, due to $\Delta H^0 > 0$, this adsorption process in the present study is endothermic, and heating is beneficial for the adsorption process. $\Delta S^0 > 0$ in the present study also indicates that the reaction process enhances the disorder degree of the solid–liquid interface, exhibiting that the adsorption process easily continues. Overall, this adsorption process was spontaneous, endothermic and entropy-driven.

3.5. The Balance of NO_3-N Removal, Ammonia Nitrogen and Nitrogen Generation

Figure S9a shows that nZVI/Zr-Ce-SBA-15 was simultaneously undergoing adsorption, reduction, and catalysis in the process of NO_3-N removal because the removal capabilities of NO_3-N using nZVI/Zr-Ce-SBA-15 are obviously higher than those when using Zr-Ce-SBA-15. Although the possible product, N_2, in the reaction process was not collected and detected, the part with insufficient total nitrogen balance is likely to be N_2 (g), and research results have showed that Fe^0 can be reduced to N_2 by NO_3-N, and a very small amount of NO_2^- is generated in the reaction process. With the progress of the reaction, NO_2^- is also reduced to N_2 or NH_4^+, and NO_2^- is the intermediate product of nZVI reducing NO_3^--N. In addition to the direct reduction function of Fe^0, it also can dissolve to produce Fe^{2+} in acidic water environment. Chen et al. [48] suggested that Fe^{2+} can significantly improve the removal rate of Fe^0 for NO_3^-, and the higher the concentration of Fe^{2+} was, the higher the removal efficiency of NO_3^- was. Because the non-acidified Fe^0 has an oxide film, the reduction rate of NO_3^- in the initial stage of the reaction was slow. Fe^{2+} converted the Fe_2O_3 oxide film on the surface of nZVI into Fe_3O_4, accelerating the transfer of electrons from Fe^0 to NO_3^-, and promoting the reduction of NO-3. Therefore, the dissolution of Fe^{2+} in the nZVI/Zr-Ce-SBA-15-NO_3-N system may indirectly accelerate or catalyze NO_3-N removal, which can be confirmed by the Fe^{2+} concentration increasing firstly and then decreasing in Figure S9b. In addition, cerium oxide is the most stable oxide among rare-earth elements. As an active site of surface, the concentration of oxygen vacancy is directly related to the catalytic performance of decorated catalysts. Based on defect chemistry, other metal ions are introduced into the oxide lattice to form solid solutions, which induce more abundant oxygen vacancies, thereby improving the migration rate of surface oxygen and lattice oxygen. Liu et al. [49] reported a promotion effect of cerium and lanthanum oxides on the Ni/SBA-15 catalyst for ammonia decomposition. Zhang et al. [50] exhibited a promoting effect of cerium doping on iron–titanium composite oxide catalysts for the selective catalytic reduction of NOx with NH_3. Combined with the published literature, the existence of Ce in nZVI/Zr-Ce-SBA-15 may act as a catalyst in the NO_3-N removal process. After NO_3-N adsorption, reduction and catalysis onto Zr-Ce-SBA-15 mesoporous materials, the proportion of N was significantly increased in comparison with before removal and pure Zr-Ce-SBA-15 mesoporous materials (Figure 11). This was indicted that the massive NO_3-N were adsorbed, reduced, and catalyzed onto Zr-Ce-SBA-15 mesoporous materials.

Figure 12 shows that the removal rate of NO_3-N by nZVI can reach 87%, and it cannot completely remove NO_3-N. This is probably due to the easy agglomeration of nZVI, as the effective active sites are reduced. nZVI/Zr-Ce-SBA-15 composites can improve the NO_3-N removal rate, as well as the NH_4^+-N and N_2 generation rate, which is because nZVI loaded onto Zr-Ce-SBA-15 as a reducing agent reduced agglomeration, providing more active sites, and thus improving the removal efficiency. In addition, Zr-Ce-SBA-15 improves the dispersion of nZVI, allowing it to better react with N_2 and enhance its selectivity. In particular, the selectivity of N_2 is 19.54% after NO_3-N adsorption onto Zr-Ce-SBA-15. Zha et al. [51] reported that NO_3-N from industrial wastewater was removed through Fe/Cu composites. A primary cell structure formed by iron–copper enhanced the effect of nZVI on NO_3-N removal. The removal NO_3-N efficiency and N_2 selectivity are 40.94% and 28.96%, respectively. There is little NO_2-N content in the process of NO_3-N removal using nZVI/Zr-Ce-SBA-15 composites. This may be because NO_2-N is only the intermediate product of NO_3-N being reduced to NH_4^+-N and will not exist stably in the reduction process. In the removal process, the removal rate of NO_3-N is greater than the generation rate of NH_4^+-N. This is because there is a certain order of reaction between the two substances. NO_3-N is first adsorbed on the surface of the composites, and then it is reduced by nZVI to NH_4^+-N. After the reaction, most of the NO_3-N removed is reduced to NH_4^+-N by nZVI, indicating that NH_4^+-N is the main product when nZVI reduces NO_3-N, which is in accordance with Song et al. [52] and Shi et al. [53]. Hwang et al. [54] found that with the increase in the pH of the reaction system, ammonium ions will discharge the solution in the form of ammonia with mechanical stirring. Chao et al. [55] found that the final product

of NO_3-N reduction by nZVI is N_2, and there is no generation of NH_4^+-N. In addition, the yield of N_2 was been improved and the present study showed the two products were more likely to coexist in the adsorption process. Referring to the works of Wang et al. [40] and Pan et al. [56], the mechanism of this adsorption process in the present study is exhibited in Figure 12.

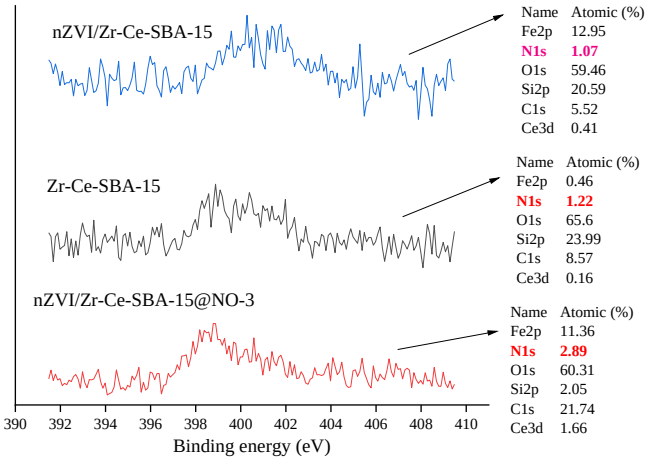

Figure 11. The XPS characterization of magnified N1S spectrogram of Zr-Ce-SBA-15, nZVI/Zr-Ce-SBA-15 and nZVI/Zr-Ce-SBA-15@NO_3-N composites.

3.6. Stability and Regeneration of nZVI/Zr-Ce-SBA-15

The desorption rate is an important index reflecting the economy of the adsorbent. Therefore, five adsorption/desorption cycle tests were conducted to study the reusability of nZVI/Zr-Ce-SBA-15 (Figure S10). The adsorption rate of nZVI/Zr-Ce-SBA-15 to NO_3-N decreased when desorbing with 0.5 mol/L HCI, while the effective removal of NO_3-N could still be maintained in the first three experiments (removal rate > 80%). After repeated desorption three times, the adsorption rate decreased significantly and tended to be stable, and the removal rate of NO_3-N was merely 65%. This may be because some H^+ occupies the surface binding sites during acid desorption. Although the treated adsorbent was washed many times to reach neutrality and for reuse, the effect of acid treatment is irreversible, resulting in the decrease in the removal rate. Another possible reason for this is that, due to incomplete acid desorption, some NO_3-N still occupied the adsorption sites, resulting in the reduction in adsorption sites. Five adsorption/desorption tests show that nZVI/Zr-Ce-SBA-15 composites have strong renewability in the short term, and repeated recycling will reduce its adsorption capacity.

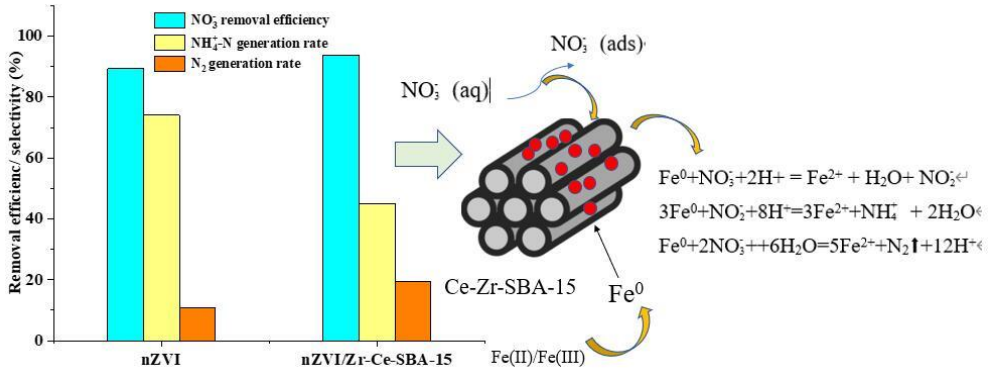

Figure 12. The efficiency/selectivity of nZVI/Zr−Ce−SBA−15 used for NO_3-N removal and its mechanism (nZVI/Zr−Ce−SBA−15 = 3 g/L; contact time = 0−8 h, temperature = 298 K and initial NO_3-N concentration = 60 mg/L).

4. Conclusions

In the present study, nZVI/Zr-Ce-SBA-15 composites were prepared and used to remove NO_3-N from simulated wastewater. The nZVI was successfully supported onto Zr-Ce-SBA-15, confirmed using XRD, FTIR, TEM, SEM–EDS, N_2 adsorption and XPS, which showed them to be ordered mesoporous materials. The ANN model was better than the RSM model. The developed ANN-GA model exhibited that the removal rate of NO_3-N by nZVI/Zr-Ce-SBA-15 reached 95.71% under the following optimal parameters: initial pH = 4.89, contact time = 62.27 min, initial NO_3-N concentration = 74.84 mg/L and temperature = 24.77. Based on the above parameters, the experimental removal rate of NO_3-N was 94.64%. Moreover, the RBF neural network further confirmed the reliability of the ANN-GA model. Pseudo-second-order kinetics can better describe the behavior of NO_3-N adsorption onto nZVI/Zr-Ce-SBA-15 composites, and this reaction was spontaneous, endothermic and entropy-driven. The process of NO_3-N adsorption onto Zr-Ce-SBA-15 composites was followed by the Langmuir model, and its maximum adsorption capacity was 47.17 mg/g. It was indirectly confirmed that the maximum removal capacity of nZVI/Zr-Ce-SBA-15 exceeded this value because the removal efficiency of NO_3-N using nZVI/Zr-Ce-SBA-15 was obviously higher than that when using Zr-Ce-SBA-15. The yield of N_2 can be improved after nZVI is supported on Zr-Ce-SBA-15, and the composites exhibited strong renewability in the short term within three cycles. The resolution of Fe ions experiments confirmed that nZVI/Zr-Ce-SBA-15 simultaneously underwent adsorption and catalysis in tprocess of NO_3-N removal. Although many methods have been used to remove NO_3-N from water, there are few studies on how to convert NO_3-N into versatile N_2. Several researchers found that the inclusion of precious metals in materials, such as Cu, Pd, Pt, etc., can significantly improve the selectivity of N_2, which is also the next direction to enhance the selectivity of nZVI/Zr-Ce-SBA-15 to N_2 in the next study.

Supplementary Materials: The following supporting information can be downloaded at: https://www.mdpi.com/article/10.3390/catal12070797/s1, Figure S1: SEM characterization of Si (a) and Zr (b) distribution of nZVI/Zr-Ce-SBA-15 composites; Figure S2 Characterization of N2 adsorption for nZVI/Zr-Ce-SBA-15 composites; Figure S3 XPS characterization of magnified Fe2p spectrogram of Zr-Ce-SBA-15 (a) and nZVI/Zr-Ce-SBA-15 (b); Figure S4. Comparison with the predicted and actual values; Figure S5 The training performance of ANN (a) and RBFNN (b); Figure S6 The correlation coefficient between target and output values (a) and the lowest MSE value in ANN model; Figure S7 The comparison of predicted and actual values by RBFNN; Figure S8 The fitting process and parameters of thermodynamics; Figure S9 The comparison of removal efficiency of NO_3-N using Zr-Ce-SBA-15 and nZVI/Zr-Ce-SBA-15 composites (a) and Fe^{2+} dissolution of nZVI/Zr-Ce-SBA-15 in solution (b) (Zr-Ce-SBA-15 or nZVI/Zr-Ce-SBA-15 = 0.15 g; initial NO_3-N concentration = 60 mg/L and initial pH = 4; temperature = 25 °C); Figure S10 The adsorption and desorption efficiencies of nZVI /Ce-Zr-SBA-15.

Author Contributions: Conceptualization, R.Z. and H.L.; methodology, H.L.; software, W.J. and W.L.; validation, R.Z., W.J. and W.L.; formal analysis, R.Z.; investigation, R.Z.; resources, R.Z.; data curation, R.Z. All authors have read and agreed to the published version of the manuscript.

Funding: This research was funded by Open Research Found of Jiangsu Province Key Laboratory of Environmental Engineering, [HX2017005] and [KF2015008].

Institutional Review Board Statement: Not applicable.

Informed Consent Statement: Not applicable.

Data Availability Statement: Not applicable.

Conflicts of Interest: The authors declare no conflict of interest.

Sample Availability: Not applicable.

References

1. Jiang, H.; Zhang, Q.; Liu, W.; Zhang, J.; Xu, Z. Isotopic compositions reveal the driving forces of high nitrate level in an urban river: Implications for pollution control. *J. Clean. Prod.* **2021**, *298*, 126693. [CrossRef]
2. Sendrowski, A.; Castaeda-Moya, E.; Twilley, R.; Passalacqua, P. Biogeochemical and hydrological variables synergistically influence nitrate variability in coastal deltaic wetlands. *J. Geophys. Res. Biogeo.* **2021**, *126*, e2020JG005737. [CrossRef]
3. Zhang, X.; Zhang, Y.; Shi, P.; Bi, Z.; Ren, L. The Deep Challenge of Nitrate Pollution in River Water of China. *Sci. Total Environ.* **2021**, *770*, 144674. [CrossRef] [PubMed]
4. Dinelli, E.; Testa, G.; Cortecci, G.; Barbieri, M. Stratigraphic and petrographic constraint to traced element and isotope geochemistry of Messinian sulphates of Tuscany. *Mem. Soc. Geol. Ital.* **1999**, *54*, 61–74.
5. Preetha, P.; Al-Hamdan, A. Integrating finite-element-model and remote-sensing data into SWAT to estimate transit times of nitrate in groundwater. *Hydrogeol. J.* **2020**, *28*, 2187–2205. [CrossRef]
6. Gu, B.; Ying, G.; Chang, S.; Luo, W.; Jie, C. Nitrate in groundwater of China: Sources and driving forces. *Glob. Environ. Chang.* **2013**, *23*, 1112–1121. [CrossRef]
7. Lundberg, J.; Weitzberg, E.; Gladwin, M. The nitrate-nitrite-nitric oxide pathway in physiology and therapeutics. *Nat. Rev. Drug Discov.* **2008**, *7*, 156–167. [CrossRef]
8. Cosby, K.; Partovi, K.; Crawford, J.; Patel, C.; Martyr, S.; Yang, B.; Waclawiw, M.; Zalos, G.; Xu, X. Nitrite reduction to nitric oxide by deoxyhemoglobin vasodilates the human circulation. *Nat. Med.* **2003**, *9*, 1498–1505. [CrossRef]
9. Zhang, F.; Yi, W.; Cao, J.; He, K.; Liu, Y.; Bai, X. Microstructure characteristics of tea seed dietary fibre and its effect on cholesterol, glucose and nitrite ion adsorption capacities in vitro: A comparison study among different modifications. *Int. J. Food Sci. Technol.* **2020**, *55*, 1781–1791. [CrossRef]
10. Babu, D.; Ravindhranath, K.; Mekala, S. Simple effective new bio-adsorbents for the removal of highly toxic nitrite ions from wastewater. *Biomass Convers. Biorefin.* **2021**, *12*, 1–13. [CrossRef]
11. Wang, Z.; Richards, D.; Singh, N. Recent discoveries in the reaction mechanism of heterogeneous electrocatalytic nitrate reduction. *Catal. Sci. Technol.* **2021**, *11*, 705–725. [CrossRef]
12. Dhakal, P.; Coyne, M.; Mcnear, D.; Wendroth, O.; Vandiviere, M.; D'Angelo, E.; Matocha, C. Reactions of Nitrite with Goethite and Surface Fe (II)-Goethite Complexes. *Sci. Total Environ.* **2021**, *782*, 146406. [CrossRef] [PubMed]
13. Crane, R.; Scott, T. Nanoscale zero-valent iron: Future prospects for an emerging water treatment technology. *J. Hazard. Mater.* **2012**, *211–212*, 112–125. [CrossRef] [PubMed]
14. Zhou, Y.; Li, X. Green synthesis of modified polyethylene packing supported tea polyphenols-NZVI for nitrate removal from wastewater: Characterization and mechanisms. *Sci. Total Environ.* **2022**, *806*, 150596. [CrossRef]
15. Zhang, Y.; Li, Y.; Li, J.; Hu, L.; Zheng, X. Enhanced removal of nitrate by a novel composite: Nanoscale zero valent iron supported on pillared clay. *Chem. Eng. J.* **2011**, *171*, 526–531. [CrossRef]
16. Song, L.; Wang, H.; Rui, C.; Liu, Q.; Zhang, Y.; Cheng, Y.; He, J. Preparation and properties of aflatoxins imprinted polymer grafted onto the surface of mesoporous silica SBA-15 functionalized with double bonds. *J. Sep. Sci.* **2021**, *44*, 4181–4189. [CrossRef]
17. Yuan, S.; Wang, M.; Liu, J.; Guo, B. Recent advances of SBA-15-based composites as the heterogeneous catalysts in water decontamination: A mini-review. *J. Environ. Manag.* **2020**, *254*, 109787. [CrossRef] [PubMed]
18. Voort, P. An Overview of the Challenges and Progress of Synthesis, Characterization and Applications of Plugged SBA-15 Materials for Heterogeneous Catalysis. *Materials* **2021**, *14*, 5082–5090.
19. Chen, S.; Jang, L.; Cheng, S. Synthesis of Zr-incorporated SBA-15 mesoporous materials in a self-generated acidic environment. *Chem. Mater.* **2004**, *16*, 4174–4180. [CrossRef]
20. Ruan, J.; Li, J.; Shen, Z.; Gu, J.; Li, H.; Sun, X.; Wang, L. Synthesis and Morphological Control of Zr-Ce-SBA-15 Mesoporous Materials. *Rare Met. Mater. Eng.* **2011**, *40*, 6–15.
21. Tang, L.; Tang, J.; Zeng, G.; Yang, G.; Xie, X.; Zhou, Y.; Pang, Y.; Fang, Y.; Wang, J.; Xiong, W. Rapid reductive degradation of aqueous p-nitrophenol using nanoscale zero-valent iron particles immobilized on mesoporous silica with enhanced antioxidation effect. *Appl. Surf. Sci.* **2015**, *333*, 220–228. [CrossRef]
22. Zhang, R.M.; Li, J.S.; Guan, Y.; Qi, L. Reduction of Trinitrotoluene by Nanoscale Zero-Valent Iron Confined in Mesoporous Channels. *Technol. Water Treat.* **2017**, *43*, 19–23. (In Chinese)
23. Xiang, G.; Long, S.; Liu, H.; Wu, X. Cd (II) removal from aqueous solutions by pomelo peel derived biochar in a permeable reactive barrier: Modelling, optimization and mechanism. *Mater. Res. Express* **2021**, *8*, 115508. [CrossRef]
24. Ayala, H.; Habineza, D.; Rakotondrabe, M.; Coelho, L. Nonlinear black-box system identification through coevolutionary algorithms and radial basis function artificial neural networks. *Appl. Soft. Comput.* **2019**, *87*, 105990. [CrossRef]
25. Hong, H.; Zhang, Z.; Guo, A.; Shen, L.; Sun, H.; Liang, Y.; Wu, F.; Lin, H. Radial basis function artificial neural network (RBF ANN) as well as the hybrid method of RBF ANN and grey relational analysis able to well predict trihalomethanes levels in tap water. *J. Hydrol.* **2020**, *591*, 125574. [CrossRef]
26. Lina, A.; Calzada, R.; García, A.; Tatiana, E. TiO_2, SnO_2 and ZnO catalysts supported on mesoporous SBA-15 versus unsupported nanopowders in photocatalytic degradation of methylene blue. *Micropor. Mesopor. Mat.* **2019**, *285*, 247–258.
27. Amr, A.; Es, B.; Mab, C.; Em, D.; Da, D. Mercury removal from aqueous solution via functionalized mesoporous silica nanoparticles with the amine compound. *Egypt. J. Pet.* **2019**, *28*, 289–296.

28. Betiha, M.; Moustafa, Y.; El-Shahat, M.; Rafik, E. Polyvinylpyrrolidone-Aminopropyl-SBA-15 schiff Base hybrid for efficient removal of divalent heavy metal cations from wastewater. *J. Hazard. Mater.* **2020**, *397*, 122675. [CrossRef]
29. Popa, A.; Sasca, V.; Verdes, O.; Barvinschi, P.; Holclajtner-Antunovic, I. Acidic and neutral caesium salts of 12-molybdophosphoric acid supported on SBA-15 mesoporous silica. The influence of Cs concentration and surface coverage on textural and structural properties. *Mater. Res. Bull.* **2014**, *50*, 312–322. [CrossRef]
30. Li, Q.; Wang, H.; Chen, Z.; He, X.; Wang, X. Adsorption-reduction strategy of U(VI) on NZVI-supported zeolite composites via batch, visual and XPS techniques. *J. Mol. Liq.* **2021**, *339*, 116719. [CrossRef]
31. Silva, F.; Silva, L.; Santos, A.; Caldeira, V.; Luz, G. Structural Refinement, Morphological Features, Optical Properties, and Adsorption Capacity of α-Ag_2WO_4 Nanocrystals/SBA-15 Mesoporous on Rhodamine B Dye. *J. Inorg. Organomet. Polym. Mater.* **2020**, *30*, 3626–3645. [CrossRef]
32. Yang, J.; Wang, S. Study on optimization of elimination effect of garlic extracts on nitrite by response surface method in salted meat. *China Condiment* **2009**, *34*, 47–51. (In Chinese)
33. Rahdar, S.; Pal, K.; Mohammadi, L.; Rahdar, A.; Kyzasg, G. Response surface methodology for the removal of nitrate ions by adsorption onto copper oxide nanoparticles. *J. Mol. Struct.* **2021**, *1231*, 129686. [CrossRef]
34. Chen, C.H.; Yang, S.H.; Chu, Y.J. Nitrite Scavenging Effect of Polyphenols from Major Small Grains in Yunnan Province. *Food Res. Dev.* **2019**, *40*, 17–23. (In Chinese)
35. Cai, J.; Zheng, P.; Qaisar, M. Prediction and quantifying parameter importance in simultaneous anaerobic sulfide and nitrate removal process using artificial neural network. *Environ. Sci. Pollut. Res.* **2015**, *22*, 8272–8279. [CrossRef]
36. Lee, S.C.; Kang, J.K.; Jang, H.Y. Multi-parameter experiments and modeling for nitrate sorption to quaternary ammonium-functionalized poly(amidoamine) dendrimers in aqueous solutions. *Int. J. Environ. Sci. Technol.* **2022**, *19*, 1–14. [CrossRef]
37. Liu, Y.; Zhang, L.Y. Implementation of BP and RBF neural network and their performance comparison. *Electron. Meas. Technol.* **2007**, *30*, 77–91. (In Chinese)
38. Yao, C.; Zhu, C. A new multi-mechanism adsorption kinetic model and its relation to mass transfer coefficients. *Surf. Interfaces* **2021**, *26*, 101422. [CrossRef]
39. Zhao, Y.; Zhu, F.; Ren, W.T. Kinetics of nitrate removal groundwater using green synthesized nanoscale zero valent iron-nickel. *Environ. Eng.* **2018**, *36*, 71–76. (In Chinese)
40. Wang, H.X.; Liao, B.; Lu, T.; Wang, J.Z.; Wei, S.M.; Liu, G. Nitrate removal from groundwater by zero-valent iron-biochar composites. *Chin. J. Environ. Eng.* **2020**, *14*, 3317–3328. (In Chinese)
41. Bhatnagar, A.; Ji, M.; Choi, Y.H.; Jung, W. Removal of nitrate from water by adsorption onto zinc chloride treated activated carbon. *Sep. Sci. Technol.* **2008**, *43*, 886–907. [CrossRef]
42. Meng, X.; Yao, L.; Jiang, W. In Situ Growth Synthesis of the CNTs@AC Hybrid Material for Efficient Nitrate-Nitrogen Adsorption. *ACS Omega* **2021**, *6*, 1612–1622. [CrossRef] [PubMed]
43. He, Z.P.; Han, M.D.; Pang, L.J. Adsorption behavior and mechanism of the bamboo-carbon for nitrate in aqueous solution. *Food Mach.* **2010**, *26*, 68–71. (In Chinese)
44. Dioum, A.; Hamoudi, S. Mono- and quaternary-ammonium functionalized mesoporous silica materials for nitrate adsorptive removal from water and wastewaters. *J. Porous Mat.* **2014**, *21*, 685–690. [CrossRef]
45. Kang, J.K.; Kin, S.B. Synthesis of quaternized mesoporous silica SBA-15 with different alkyl chain lengths for selective nitrate removal from aqueous solutions. *Micropor. Mesopor. Mat.* **2020**, *295*, 109967. [CrossRef]
46. Wang, H.; Wang, G.F.; Li, L. Study on the denitrification performance of Fe-SBA-15 mesoporous molecular sieve in the removal of nitrate nitrogen from Beijing Groundwater. *Resour. Conserv. Environ. Prot.* **2016**, *181*, 40–44. (In Chinese)
47. Aouaini, F.; Yahia, M.B.; Alanazi, M. Phenomenological statistical physics modeling of metalloporphyrins adsorption at the molecular level. *J. Mol. Liq.* **2021**, *340*, 117108. [CrossRef]
48. Chen, H.; Zhang, Y.P.; Ruan, X.H. Effect of Fe^{2+} on Nitrate Reduction Using Zero-valent Iron. *Geol. J. China Univ.* **2018**, *24*, 84–90. (In Chinese)
49. Liu, H.; Hua, W.; Shen, J. Promotion effect of cerium and lanthanum oxides on Ni/SBA-15 catalyst for ammonia decomposition. *Catal. Today* **2008**, *131*, 444–449. [CrossRef]
50. Zhang, W.; Shi, X.; Shan, Y. Promotion effect of cerium doping on iron–titanium composite oxide catalysts for selective catalytic reduction of NO_x with NH_3. *Catal. Sci. Technol.* **2020**, *10*, 648–657. [CrossRef]
51. Zha, X.S.; Feng, Z.L.; Jin, S.W. Removal of Nitrate in Water by Reduction of Iron-Based Bimetal. *Technol. Water Treat.* **2020**, *46*, 44–48. (In Chinese)
52. Song, Y.J.; Song, S.F. Preparation, characterization, and kinetics of nanoscale iron in nitrate nitrogen removal from polluted water. *Toxico. Environ. Chem.* **2015**, *97*, 379–387. [CrossRef]
53. Shi, J.; Yi, S.; He, H. Preparation of nanoscale zero-valent iron supported on chelating resin with nitrogen donor atoms for simultaneous reduction of Pb^{2+} and NO_3^-. *Chem. Eng. J.* **2013**, *230*, 166–171. [CrossRef]
54. Hwang, Y.H.; Kim, D.G.; Shin, H.S. Effects of synthesis conditions on the characteristics and reactivity of nano scale zero valent iron. *Appl. Catal. B-Environ.* **2011**, *105*, 144–150. [CrossRef]

55. Choe, S.; Chang, Y.Y.; Hwang, K.Y. Kinetics of reductive denitrification by nanoscale zero-valent iron. *Chemosphere* **2000**, *41*, 1307–1311. [CrossRef]
56. Pan, W.L.; Wu, Q.Y.; Cao, Y.P.; Zhang, X.B.; Gu, L.; He, Q. Improvement of nitrate removal and nitrogen selectivity by the synergy of nZVI/BC and (Cu-Pd)/BC. *Chem. Ind. Eng. Prog.* **2022**, *41*, 981–989.